

High piezoelectric property with exceptional stability in self-poled ferroelectric films

Received: 4 July 2024

Accepted: 20 November 2024

Published online: 30 December 2024



Lisha Liu^{1,7}✉, Jiaojiao Yi^{2,7}✉, Kun Xu^{3,4,7}, Zhen Liu¹, Mingmeng Tang¹, Le Dai¹, Xuan Gao¹, Yang Liu¹, Shuhao Wang¹, Zhang Zhang¹, Liang Shu⁵, Jing-Feng Li⁵, Shujun Zhang⁶✉ & Yaojin Wang¹✉

Ferroelectric films are highly sought-after in micro-electro-mechanical systems, particularly with the trend towards miniaturization. However, their tendency to depolarize and degradation in piezoelectric properties when exposed to packaging procedures at temperatures exceeding 260 °C remains a significant challenge. Here, we reveal the prerequisites for self-poling and leverage these insights to achieve unprecedented macroscopic performance through a two-step approach involving texture construction and hierarchical heterogeneity engineering. The significant [001] texture and fine Zr/Ti heterogeneity, facilitated by a PbO-TiO₂ buffer, enable a piezoelectric charge coefficient of 550 pC/N in self-poled Pb(Zr_{0.52}Ti_{0.48})O₃ film. This material demonstrates impressive resilience to elevated temperatures up to 300 °C, experiencing less than a 16% degradation in performance. Our approach can be extended to other ferroelectric systems, offering an innovative solution for high-temperature packaging and harsh environments in practical electro-mechanical applications.

Ferroelectric films are critical components for micro-electro-mechanical systems (MEMS) due to their exceptional piezoelectric properties, enabling greater actuation ranges and more sensitive detection elements^{1–4}. The pursuit of higher piezoelectric response is driven by the demands of next-generation devices with enhanced sensing capability and the trend toward miniaturization. Thickness-mode devices, leveraging the direct piezoelectric effect (piezoelectric charge coefficient $d_{33,d}$), are particularly important for miniaturization, meeting the requirements of modern pressure sensors, wearable medical devices, and energy harvesters^{5–9}. Lead zirconate titanate, Pb(Zr,Ti)O₃ (PZT), is the most widely used ferroelectric material in commercial applications, renowned for its reliability and cost-effective manufacturing. However, PZT films exhibit a wide range of

documented $d_{33,d}$, ranging from 80 to 230 pC/N after poling^{10–12}, which are significantly lower and more dispersed compared to bulk PZT ceramics. In PZT ceramics, $d_{33,d}$ typically exceeds 250 pC/N and can reach over 700 pC/N with advanced texturing¹³. This disparity motivates efforts to enhance $d_{33,d}$ in PZT films.

The practical application of PZT films typically involves deposition onto silicon wafers or other substrates, which can induce substrate clamping effects and severe depoling fields, compromising the initial poling state and reducing $d_{33,d}$ ¹⁴. In addition, the high-temperature treatments (usually exceeding 260 °C, Fig. 1a) required in the MEMS packaging process, negatively impact the functionality of ferroelectric films. Very limited ferroelectric films can endure such high temperatures without experiencing depoling, posing an

¹School of Materials Science and Engineering, Nanjing University of Science and Technology, Nanjing, Nanjing, China. ²Laboratory of Advanced Multi-component Materials, School of Mechanical Engineering, Jiangsu University of Technology, Changzhou, China. ³Department of Mechanical Engineering, Stanford University, Palo Alto, US. ⁴National Center for Electron Microscopy in Beijing, School of Materials Science and Engineering, Tsinghua University, Beijing, China. ⁵State Key Laboratory of New Ceramics and Fine Processing, School of Materials Science and Engineering, Tsinghua University, Beijing, China. ⁶Institute of Superconducting and Electronic Materials, Faculty of Engineering and Information Sciences, University of Wollongong, Wollongong, Australia. ⁷These authors contributed equally: Lisha Liu, Jiaojiao Yi, Kun Xu. ✉e-mail: lishaliu@njjust.edu.cn; yijiaojiao2006@163.com; shujun@uow.edu.au; yjwang@njjust.edu.cn

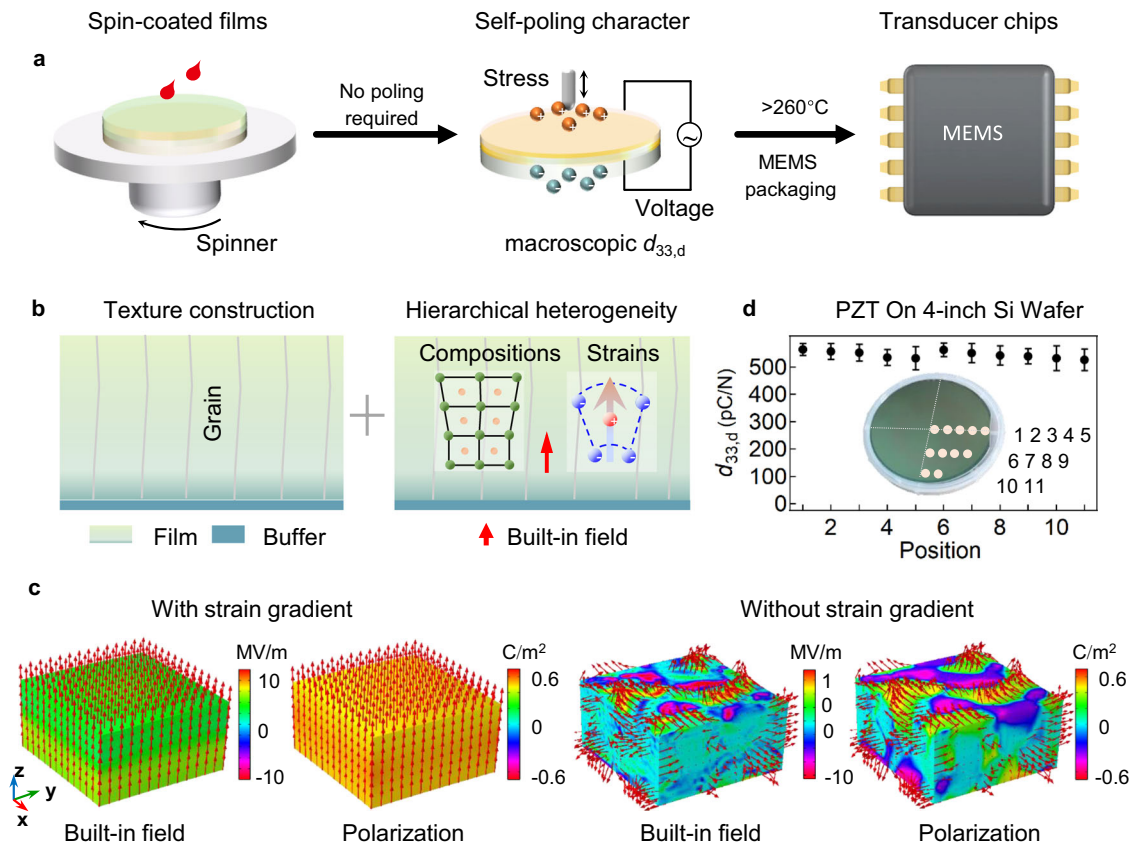


Fig. 1 | Self-poling and outstanding macroscopic piezoelectric performance in spin-coated $\text{Pb}(\text{Zr},\text{Ti})\text{O}_3$ (PZT) films. **a** The concept of self-poling, which leverages macroscopic direct piezoelectricity ($d_{33,d}$) achieved in spin-coated ferroelectric films, has the potential to revolutionize commercial materials for micro-electro-mechanical systems (MEMS) applications. **b** The two-step approach for inducing self-poling in ferroelectric films during fabrication involves texture construction and hierarchical heterogeneity engineering. **c** Simulated driving fields for self-

poling (i.e., polarization alignment) induced by strain gradients, a typical form of hierarchical heterogeneity, compared to random fields and polarizations in films with strain homogeneity. The simulated component has a thickness of 100 nm, equivalent to a single spin-coated layer. **d** $d_{33,d}$ in self-poled PZT films deposited on the 4-inch silicon wafer, employing forty repeated spin coatings. The error bars represent different measurements, and the inset is a photograph showing the as-fabricated large-area 4 μm -thick PZT films.

unresolved fundamental challenge and hindering their widespread integration into MEMS. Therefore, developing strategies to eliminate external poling procedures is essential for developing ferroelectric films that remain unaffected by substrate clamping or high-temperature packaging.

Self-polarization in ferroelectric films has been recognized in prior studies with various mechanisms being proposed, such as the Schottky barrier at the electrode/film interface¹⁵, Pb excess in PZT¹⁶, texture construction¹⁷, designed sub-micron scale composition gradient^{18,19}, and bulk/surface defects^{20,21}. However, contradictory conclusions have been documented. For instance, some studies report stronger self-polarization in thicker films, while others claim an interfacial effect that reinforces in thinner films¹⁵. Some studies emphasize the significance of Pb excess for self-polarization¹⁶, while most link it to texturing by using PbO as a buffer^{22–24}. Even so, the relationship between texture and self-polarization remains unclear; otherwise, epitaxial films (representing an extreme case of texture) would always demonstrate self-polarization, but this is not the case. Defects, lacking direct visualizations or quantifications, add to the mystery. The ongoing controversy surrounding self-polarization has made the concept less practical and has yet to lead to a major breakthrough in achieving macroscopic piezoelectric performance in PZT or any other films.

Achieving desirable macroscopic performance requires the prerequisites of self-polarization, also termed self-poling in this study, which necessitates comprehensive designs. Successfully implementing self-poling will enable a reliable and enhanced

macroscopic $d_{33,d}$ without the need for external poling procedures, thus addressing issues of inferior piezoelectricity and packaging-related challenges faced by ferroelectric films in MEMS application and commercialization.

Results

Macroscopic piezoelectricity in self-poled ferroelectric films

We propose a two-step approach to self-pole ferroelectric films during fabrication, with the specific intention to attain an effective macroscopic $d_{33,d}$: (i) constructing textures or promoting epitaxial crystal growth within films, as it was hypothesized that polycrystalline materials could average out any anisotropic driving forces for self-poling; and (ii) engineering a fine hierarchical heterogeneity in the thickness direction induced by compositions, lattices, strains, or charges (e.g., arising from defects), thereby ensuring an anisotropic driving force across the film bulk for polarizations alignments (Fig. 1b). Notably, the second step is essential for implementing this approach, as epitaxial growth (an extreme case of texture) does not necessarily lead to self-poling.

The phase-field simulation was used to demonstrate the necessity of achieving hierarchical heterogeneity along the film thickness direction through the introduction of a strain gradient, a typical heterogeneity described above, in a ferroelectric layer sized $100 \times 100 \times 50 \text{ nm}^3$ (Fig. 1c). The simulations show a significant driving field generated from the strain gradient, aligning the spontaneous polarizations to the out-of-plane direction (Fig. 1c, left two panels). This is in stark contrast to scenarios lacking a strain gradient, where

simulated random fields result in a random distribution of polarization (Fig. 1c, right two panels). A similar phenomenon has been observed in theoretical simulations, where a constructed $\text{Pb}(\text{Zr}_{0.53}\text{Ti}_{0.47})\text{O}_3/\text{Pb}(\text{Zr}_{0.2}\text{Ti}_{0.8})\text{O}_3$ structure produces large in-plane strains at the interfaces²⁵. This leads to a competition between bulk and interfacial energies, ultimately facilitating polarization alignment near interface regions. Experimentally, 50 nm $\text{Pb}(\text{Zr}_{0.8}\text{Ti}_{0.2})\text{O}_3/50$ nm $\text{Pb}(\text{Zr}_{0.2}\text{Ti}_{0.8})\text{O}_3$ ¹⁸ and 300 nm $\text{Pb}(\text{Zr}_{0.8}\text{Ti}_{0.2})\text{O}_3/300$ nm $\text{Pb}(\text{Zr}_{0.52}\text{Ti}_{0.48})\text{O}_3/300$ nm $\text{Pb}(\text{Zr}_{0.2}\text{Ti}_{0.8})\text{O}_3$ ¹⁹ films confirm the existence of internal fields, as evidenced by offsets in their ferroelectric loops. However, the impact of a designed sub-micron scale composition gradient is largely confined to interfaces, resulting in rarely reported or insufficient macroscopic piezoelectricity for practical applications.

In this study, a single-composition PZT with Zr:Ti = 52:48 was chosen to experimentally demonstrate the validation of the proposed two-step approach for achieving self-poling and enhanced macroscopic piezoelectricity. The choice was made for several reasons: (i) texture construction in PZT films has been recognized as straightforward and simple^{22,23}; (ii) Ti-rich composition nucleates and grows more easily than Zr-rich composition in PZT due to the lower crystallization energy of PbTiO_3 ²⁶, which could facilitate composition-based hierarchical heterogeneity. This composition heterogeneity can result in strain gradients due to lattice mismatch, as will be experimentally demonstrated below; (iii) a composition near the morphotropic phase boundary (MPB) is expected to enhance the piezoelectric property. Employing a simple and industrially scalable spin-coating method to fabricate PZT films, with constructed significant texture and Zr/Ti heterogeneity in each layer, we obtained $d_{33,d}$ up to 550 pC/N in large-area self-poled PZT films on the 4-inch silicon wafer as shown in Fig. 1d. Detailed information regarding the instrumentation used for measuring the $d_{33,d}$ and its validation can be found in the Methods, Supplementary Fig. 1 and Supplementary Movie. 1. Notably, wafer-sized and diced PZT samples exhibit negligible difference in $d_{33,d}$, as observed across dozens of samples.

Connection between texture and piezoelectricity

Mixed lead oxide (PbO) and titanium oxide (TiO_2) in various ratios, which are well-suited for the solution-based spin-coating method, were employed as buffer layers to comprehensively tailor the film textures. To start with, a texture transition from [001], [111], to [011] by adjusting the PbO- TiO_2 buffer ratio from 100:0 to 0:100 (Supplementary Fig. 2) was constructed. The Lotgering factor of [001]-textured films can reach a maximum of nearly 100%, while those of [111] and [011] textures are only 70% and 40%, respectively. It is obvious that the texture degree and piezoelectric performance are positively correlated, with smaller values observed at the texture transition point where a lower texture is present (Supplementary Fig. 2).

For [001] textured PZT films, PbO- TiO_2 buffers with an 83:17 ratio of 0 to 5 layers (10 nm per layer) are further evaluated to effectively modify the texture degree of this film with a thickness of 1 μm (Fig. 2a). The X-ray diffraction (XRD) patterns demonstrate a clear (001) grain orientation preference with PbO- TiO_2 buffers, showing pronounced (001) and (002) reflections. The calculated [001] texture Lotgering factors for PZT films with 0–3 buffer layers were approximately 53.0, 90.0, and 93.0%, corresponding to $d_{33,d}$ of -60 ± 10 , 130 ± 18 , and 350 ± 29 pC/N, respectively. Note that further increasing the number of buffer layers reduces the texture to 85.5% and deteriorates the $d_{33,d}$ as measured for more than a dozen samples.

Furthermore, by routinely inserting optimized 30 nm PbO- TiO_2 for every five PZT layers, we achieved increased [001] Lotgering factors measuring at 85.8, 93.0, 99.8, 98.4, and 98.9% for high-quality crack-free PZT films with thickness ranging from 0.5 to 4 μm , respectively (Supplementary Fig. 3). As the Lotgering factor approaches roughly 100%, the $d_{33,d}$ value significantly increases from 310 to 550 pC/N, as shown in Fig. 2b. Given that $d_{33,d} = 2P_{\text{rem}}\epsilon Q_{33}$ ²⁷, the exceptional $d_{33,d}$ values are attributed to the large remnant polarization (P_{rem}) and dielectric constant (ϵ). These parameters range from 10–27 $\mu\text{C}/\text{cm}^2$ at 200 kV/cm and 1610–2180 at 1 kHz (Supplementary Figs. 4–6) and are generally consistent with those reported in the

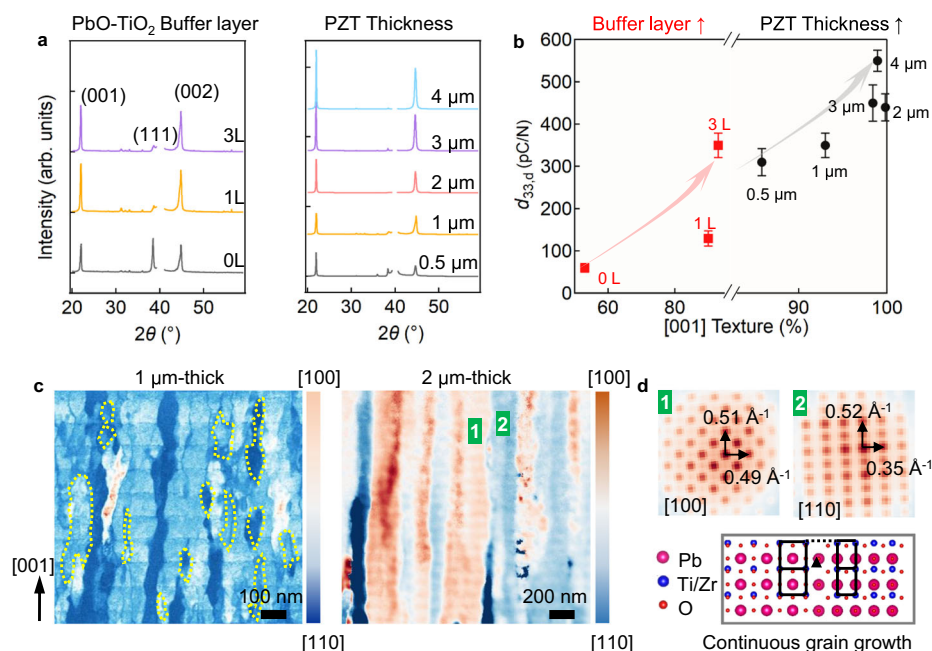


Fig. 2 | Structural characterization of textured $\text{Pb}(\text{Zr},\text{Ti})\text{O}_3$ (PZT) films. **a** The plot of theta-omega XRD scan for 1 μm film with different numbers of buffer layers, and for films with different thicknesses on 3 buffer layers. **b** Macroscopic $d_{33,d}$ as a function of texture degree, which is optimized through the numbers of buffer layer and film thicknesses. The error bars originate from multiple samples. **c** Grain mapping by diffraction under nanobeam mode across the film with brightly

contrasting stripe patterns penetrating the 1 μm (left) and 2 μm -thick (right) PZT films. The color scale bars represent in-plane grain orientation, which may vary from sample to sample depending on the regions outside the 4-inch film. **d** Nano-diffraction patterns of adjacent [100] and [110] grains (above), the schematic illustration of the twisted grains (bottom), demonstrating the interfacial structure across the twisted boundaries.

literature^{2,28}. In addition, the converse piezoelectric coefficient $d_{33,c}$, measured by a laser scanning vibrometer, ranges from 293 to 602 pm/V at a 4 V bias with a frequency of 1 kHz, showing a good consistency with $d_{33,d}$ (Supplementary Fig. 7).

Of particular importance is that using sole PbO buffer (i.e., without TiO₂) yields 98.3% [001] texture in PZT films but less reliable macroscopic piezoelectricity (i.e., only one-third out of a dozen samples present $d_{33,d}$). Thus, the addition of TiO₂ in the buffer—a straightforward process in a solution-based method like spin-coating—is crucial for the stabilization of macroscopic piezoelectricity, i.e., the self-poling feature. This is achieved by impacting the initiation of hierarchical heterogeneity in the two-step approach, a topic that will be discussed further in the following session.

Among the aforementioned methods for enhancing texture, increasing film thickness is the most counterintuitive, contradicting expectations for a discontinuous layer-by-layer deposition process. To get visualized insights, the grains across the entire as-prepared PZT film with different thicknesses were analyzed using diffraction patterns via the four-dimensional scanning transmission electron microscopy (4D-STEM) technique in nanobeam mode. Figure 2c presents a reconstructed grain map with obvious stripe grains extending throughout the entire thickness of the film from the bottom electrode. Notably, a significant number of small grains are observed in the 1 μm film, in contrast to the 2 μm film (Fig. 2c left, yellow dashed circles), suggesting a continuous refinement of grain orientation with increasing annealing times and grain coalescence and growth. There is also a significant in-plane grain orientation variation, as indicated by distinct diffraction patterns in two grains (Fig. 2d, top), a broad (002) reflection rocking curve, and an elongated (113) reflection ring from reciprocal space mapping (RSM) (Supplementary Fig. 8). The sharp lattice mismatch at grain interfaces, as depicted by the schematic unit cell (Fig. 2d, bottom), is expected to facilitate the uninterrupted grain growth in the out-of-plane direction across different layers. Moreover, in-plane grain twisting also reinforces atomic polarizations near the grain interface through out-of-plane tension, as evidenced by the STEM high-angle annular dark-field (STEM-HAADF) image (Supplementary Fig. 9). This tension may also prevent the generation of depoling fields in the film upon subjecting to environmental fluctuations, including temperature and electric field. This, in turn, stabilizes self-poling characteristics.

Hierarchical heterogeneity arising from compositions

Energy dispersive X-ray spectrum (EDXS) analysis is employed to investigate PZT films buffered by PbO-TiO₂ (Fig. 3). Figure 3a depicts that the concentration of Zr largely increases at the top of each layer, while the concentration of Ti reduces at these positions. In contrast, Pb distribution remains relatively uniform across different layers. The intensity plot of the line profile extracted from the element maps, as shown in Fig. 3b, further demonstrates this periodic variation in Zr/Ti elements. The Zr/Ti ratio, as determined from the EDXS, smoothly changes from the nominal composition 52:48 to as large as 70:30 (Zr-rich region, red dashed line in Fig. 3b) and 30:70 (Ti-rich region, orange dashed line in Fig. 3b). This significant composition gradient within each film layer, as shown in Fig. 3c, is caused by the addition of TiO₂ in the buffer layer, which is routinely applied every five PZT layers. This gradient is further reinforced by the easier nucleation and growth of the Ti-rich component in a perovskite structure regime.

Atomic-scale STEM-HAADF images of Zr-rich and Ti-rich regions in each 100 nm-thick individual layer can be obtained (Fig. 3d, e). The representative statistical c/a ratio for Zr-rich and Ti-rich regions (with estimated Zr/Ti ratios of 70:30 and 30:70, respectively) were calculated from more than two dozen of HAADF images, yielding values of 0.994 versus 1.024, showing an increase towards the PbTiO₃ end member. This is consistent with previously reported c/a ratios for thick Pb(Zr₃₀Ti₇₀)O₃ and Pb(Zr₇₀Ti₃₀)O₃ films on silicon substrate

(Supplementary Table 1). As the Zr/Ti composition gradually transitions from 30:70 to the nominal 52:48 and then to 70:30, as identified from the EDXS spectra (Fig. 3b), a corresponding smooth transition in the c/a ratio within each 100 nm layer is expected. Therefore, a strain gradient with a maximum value reaching ~3% can be induced by Zr/Ti segregation (i.e., the composition gradient) in each PZT layer. The magnitude of this strain aligns with that introduced in the phase field simulation, as shown in Fig. 1. By coinciding with the [001] texture, the built-in field in each layer, as described in the simulation, aligns in the same direction and points towards the film surface, leading to a synergistic effect for self-poling with both texture and anisotropic driving force. Notably, the films experience overall thermal stress due to the mismatch in thermal expansion coefficients between the substrate (Si - $2.6 - 4 \times 10^{-6} \text{ K}^{-1}$) and the film (PZT - $5.5 \times 10^{-6} \text{ K}^{-1}$)²⁹. However, the c/a ratios at different Ti-rich regions (0.5, 0.9, and 1.2 μm away from the bottom electrode, Supplementary Fig. 10) are similar, excluding macroscopic thermal strain as an anisotropic factor for polarization alignments.

The discernible positions of the *A*-site (Pb) and *B*-site (Zr and Ti) atomic columns can be used to quantify the displacement of *B*-site cations relative to *A*-site cations (i.e., localized polarization). As shown in the polarization maps (Fig. 3f, g, left), the polarization orientations within both Zr- and Ti-rich regions exhibit out-of-plane tendency, coinciding with the [001] driving force and texture of the film. However, Fig. 3f shows certain antiparallel nano-domains within the Zr-rich regions, likely due to the antiferroelectric nature of PbZrO₃ (indicated by black dashed lines). This antiferroelectric characteristic is observed to reduce the polarization alignment strength (Fig. 3f) in the Zr-rich regions compared to that in the Ti-rich regions. Furthermore, it is found that the strong polarization alignment is largely correlated with their localized c/a ratio, particularly in the Ti-rich regions. For instance, at Ti-rich regions with more random polarization distribution (such as those near grain boundaries), the c/a ratio decreases from the aforementioned 1.024 to 0.996. This indicates a normal Poisson's effect as constrained by the PbZrO₃ unit cells (Supplementary Fig. 11) in some localized regions, similar to what has been observed in epitaxial grown thin superlattices such as 4 nm Pb(Zr₆₅Ti₃₅)O₃/4 nm Pb(Zr₃₀Ti₇₀)O₃, of which the c/a ratio shifts from 1.016 to 0.987 due to lattice constrain and Poisson's effect³⁰. These reflect the complexity of localized lattice structures in polycrystalline textured films, especially those with elemental transitions and polarization alignment, as observed here.

In addition, the histograms of the displacement magnitude in the two different regions (Fig. 3f, g, right) also illustrate decreased polarization (~17.7 pm) within the Zr-rich area compared to the Ti-rich region (~20.9 pm). This also results in a gradual decrease of the net out-of-plane polarization as the Zr content increases within each layer, coinciding with the aforementioned composition and strain gradients.

The strong alignment of polarization along the thickness direction in its as-prepared state is further confirmed by piezoresponse force microscopy (PFM), which reveals only upward polarizations (Supplementary Fig. 12). Notably, due to the highly aligned polarizations, both the localized switching spectra through the PFM tip (SSPFM) and the macroscopic polarization-electric field (P - E) hysteresis loops exhibit visible asymmetry, resulting in positive internal bias. However, this internal bias significantly reduces, and some even diminish to a negligible level with increasing applied field, as observed in both SSPFM (Supplementary Fig. 13) and P - E (Supplementary Fig. 5) curves. This behavior differs from the previously reported fixed internal bias associated with self-polarization induced by macroscopic compositional gradient¹⁸, interfacial pinning²⁸, or defect dipoles^{21,31}, suggesting a relative ease of polarization switching in the studied self-poled films. Nevertheless, the stabilized and significant upward self-alignment of the polarizations is reflected by the very large initial polarization of up to ~15 μC/cm², which appears as an offset on the polarization axis in the P - E loops during the first measurement cycle.

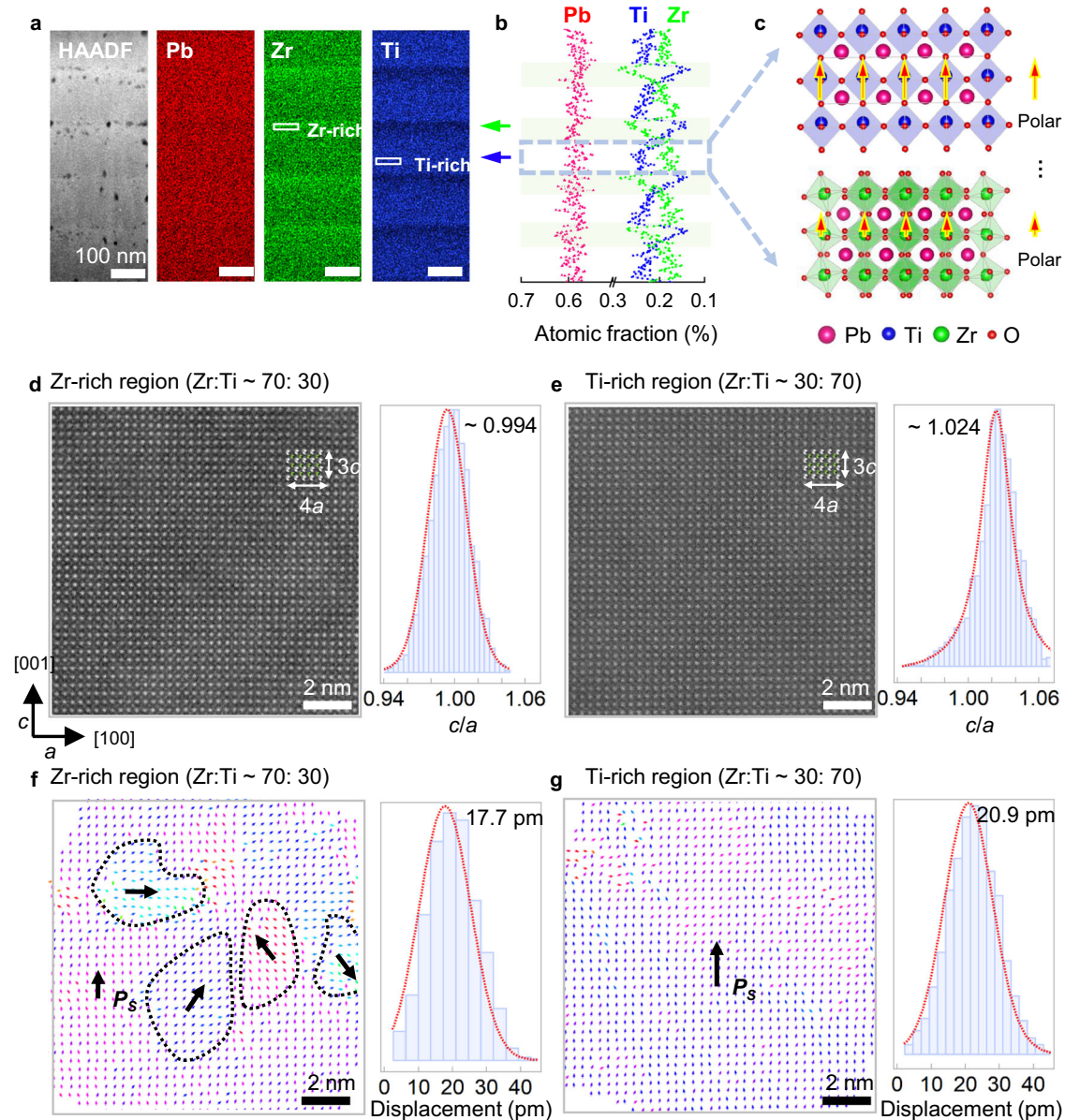


Fig. 3 | Composition and atomic-scale analysis. **a** Cross-sectional scanning transmission electron microscopy image indicates layer-by-layer growth of the prepared film with the maps of different cation elements, Pb, Zr, and Ti. Each PZT layer is approximately 100 nm. **b** Quantified atomic fractions of A- and B-site elements. The maximum composition variation, as indicated by Zr/Ti could be from 70:30 to 30:70. **c** Crystallographic structures at Zr- and Ti-rich regions in a layer as

marked by the rectangle with varying polarization magnitude. **d, e** Atomic-resolution images at Zr-rich and Ti-rich regions. Images on the right side are histograms of the c/a ratio at respective regions. **f, g** The maps of atomic-scale polarization at Zr-rich and Ti-rich regions as calculated from the A- and B-site atomic positions in corresponding Atomic-resolution images. Images on the right side are histograms of the displacement magnitude at respective regions.

To underscore the significance of composition gradient (resulting from Zr/Ti segregation) and the subsequent strain gradient at the nanoscale on impacting the macroscopic performance, we investigated two types of films as comparative cases: (i) textured PZT films with suppressed Zr/Ti segregation by compensating annealing (see methods), and (ii) non-textured PZT films with suppressed Zr/Ti segregation. These two films exhibit macroscopic piezoelectric coefficients of below 100 pC/N or approximately 0 (Supplementary Fig. 13), much smaller than the 550 pC/N we achieved in the studied films. It validates the necessity of composition gradient as a form of hierarchical heterogeneity, in the proposed two-step approach. This also explains the less reliable macroscopic $d_{33,d}$ in solely PbO-buffered PZT films, as Zr/Ti segregation is less predictable in these films.

The Zr/Ti compositional gradients, commonly observed in PZT films, are believed to negatively impact both film quality and

piezoelectric performance, as previously reported²⁶. These gradients lead to compositional deviations from the desired MPB, which generally yields optimal performance. Therefore, efforts are typically made to minimize or eliminate undesired changes in the Zr/Ti ratio to achieve optimal piezoelectric properties. However, even at the precise MPB, films with the same composition often exhibit much lower $d_{33,d}$ values compared to their bulk counterparts (200 vs 500 pC/N). This reduction is ascribed to partial depoling after the standard poling procedure due to a larger depolarization field in thinner film or substrate clamping, unlike bulk counterpart³². In contrast, films engineered with nanoscale elemental segregation, as studied here, exhibit self-poling characteristics, allowing them to largely avoid both poling and partial depoling, resulting in piezoelectric response closer to that of bulk PZTs.

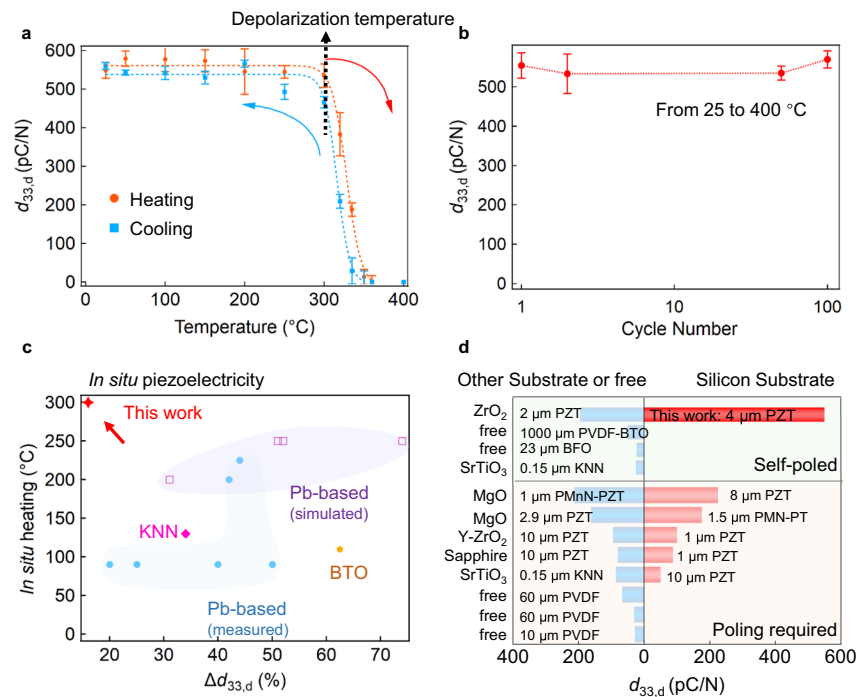


Fig. 4 | Temperature stability and service features of self-poled Pb(Zr,Ti)O₃ (PZT) films. **a** Temperature-dependence of $d_{33,d}$ in self-poled PZT films. **b** $d_{33,d}$ after different numbers of heating and cooling cycles to 400 °C (above its depolarization temperature). The data in this study are for 4 μ m-thick PZT films. The error bars represent different measurements. **c** Piezoelectric property variation versus in situ heat treatment temperature, comparing the current film to other ferroelectric films. The comparison involves piezoelectricity described by parameters such as

$d_{33,d}$, d_{31} , or $-e_{31}$, since $d_{33,d}$ is yet to be investigated in many ferroelectric thin films. **d** $d_{33,d}$ achieved in self-poled PZT films compared to other representative ferroelectric films. Notably, the graph exclusively features ferroelectric films and the small signal direct piezoelectric charge coefficient, $d_{33,d}$. The abbreviations PVDF, BTO, BFO, KNN, PMN, and PMnN denote polyvinylidene difluoride, BaTiO₃, BiFeO₃, (K,Na)NbO₃, Pb(Mg, Nb)O₃, and Pb(Mn, Nb)O₃, respectively.

Temperature stability and service features

The measured piezoelectricity of the as-prepared PZT film underscores its inherent self-poling characteristics, which can be corroborated by the complete depoling of the sample above 350 °C, followed by a full recovery as the temperature decreases to its depolarization temperature of 300 °C during the downward temperature sweep (Fig. 4a). This coincides with the complete recovery of the film phase, as demonstrated by the Raman spectra (Supplementary Fig. 14). Remarkably, the studied PZT film exhibits a piezoelectric property variation ($\Delta d_{33,d}/d_{33,d}$) below 16% across a broad temperature range up to 300 °C, accompanied by a negligible thermal hysteresis during both upward and downward temperature sweeps. This is demonstrated for all films with thicknesses ranging from 0.5 to 4 μ m, showing $\Delta d_{33,d}/d_{33,d}$ ranging from 10% to 16% (Supplementary Fig. 15). In addition, the film displays excellent thermal fatigue resistance and retains performance recovery even after undergoing more than 10² heating and cooling cycles up to 400 °C (above its depolarization temperature), as shown in Fig. 4b.

Notably, the piezoelectric response typically increases with increasing temperature due to the temperature-dependent dielectric constant, ϵ . In this study, the dielectric constant and remnant polarization exhibit opposite trends as a function of temperature— ϵ increases, while P_{rem} decreases (Supplementary Figs. 4 and 6). This may contribute to the exceptional temperature stability of $d_{33,d}$ as described by the equation $d_{33,d} = 2P_{\text{rem}}\epsilon Q_{33}$ (where Q_{33} is the electrostrictive coefficient, typically insensitive to temperature). Moreover, it is observed that annealing in the atmosphere with increased oxygen partial pressures significantly deteriorates the stability, primarily due to the reduced oxygen vacancies, indicating p -type conduction in the studied PZT (Supplementary Figs. 16, 17). Thus, the electrical transport behavior may alter the built-in fields in the film at elevated temperatures, thereby affecting their temperature stability.

The demonstrated exceptional temperature stability, and wide operating temperature range of the piezoelectricity in self-poled PZT films underscore its suitability for applications in sensors or actuators operating at elevated temperatures. This is crucial given the widespread use of electromechanical devices across a broad temperature range. In Fig. 4c, thermal instability of lead-based and lead-free inorganic films (ferroelectric film systems under in situ measurements are involved) as a function of in situ temperature are compared^{33–35}. Notably, the studied PZT shows prominent temperature stability, in contrast to the piezoelectricity described by d_{31} , $-e_{31}$, and/or $d_{33,d}$, since the latter is yet to be investigated in many ferroelectric films.

Within the board temperature range, the studied PZT films exhibit small-signal direct piezoelectricity, $d_{33,d}$, surpassing those of the most actively researched and/or commercially available ferroelectric films to date (Fig. 4d)^{10–12,17,36–42}. The achieved value of 550 pC/N is more than double the highest value of 230 pC/N documented for PZT films on silicon or other substrates^{10,43}. It should be noted that (i) previously reported self-poled ferroelectric films warrant in-depth investigation on their macroscopic $d_{33,d}$ ^{18,19,21,31}; (ii) the reported $d_{33,c}$ values of -200 – 400 pm/V for the converse piezoelectric effect in PZT films, attributes to the substantial domain switching under electric stimuli up to 120 V⁴⁴, which is beyond the practical several volts stimulus in a MEMS device. These films may exhibit different behavior in terms of their direct piezoelectric coefficients after poling, which may experience severe depoling.

Discussions

To summarize, self-polarization, feasible texture construction, and elemental segregation have been recognized in PZT films and other materials. Some studies have vaguely and intuitively suggested a correlation between them, but often lack clear visualization or quantification. Leveraging the strategy of the two-step approach and its

experimental validation, we unambiguously demonstrate the simple rules for designing self-poling in ferroelectric films with superior macroscopic piezoelectric performance, achieved through texture construction and hierarchical heterogeneity. This is validated not only for the Si substrate but also on a range of other substrates, including Mica and ZrO_2 (Supplementary Fig. 18).

It is evident that higher texture benefits macroscopic performance; for instance, increasing the texture Lotgering factor from below 90% to 93% doubles the $d_{33,d}$ at the same PZT thickness, and a value of 550 pC/N is achieved when the texture Lotgering factor approaches 100%. Future work should, therefore, specifically focus on optimizing the texture degrees. Another key challenge is to engineer hierarchical heterogeneity, essentially ensuring an anisotropic driving force for polarization alignment. It is achieved by promoting a nanoscale composition gradient (specifically Zr and Ti) in the studied PZT. This nanoscale composition regulation can be extended to other single-composition or mixed cation compounds, such as $\text{Ba}(\text{Zr}, \text{Ti})\text{O}_3$ with Zr/Ti similar to this work, or BNT with Na/Ti showing different cation weights and valence^{21,45}.

Remarkably, we aim to attain direct piezoelectricity, $d_{33,d}$, particularly merits thickness-mode MEMS devices, reaching exceptional levels between 310 and 550 pC/N with varying film thicknesses. The high $d_{33,d}$ values and its exceptional temperature stability, combined with the self-poling feature, overcome the limitations associated with poling challenges, high-temperature packaging, and high-temperature shocks in harsh environments, particularly in the ferroelectric film-based thickness-mode MEMS devices. While these properties open new research avenues for ferroelectric films, integrating the current PZT films into MEMS devices will require additional transfer procedures due to their high processing temperatures (750 °C). Reducing this temperature below 450 °C would better align with standard MEMS fabrication platforms. Nevertheless, these films offer a promising prototype for the evaluation of stability upon exposure to reactive ions and/or RF plasma used in MEMS platforms. Advances in simplified thickness-mode MEMS designs, self-poling, and unprecedented $d_{33,d}$ hold significant potential to facilitate industry progress.

Methods

Film fabrication

The films in this study were fabricated using the spin-coating method on Si/Pt substrates. Initially, precursor solutions were prepared, including PbO , TiO_2 , PbZrO_3 , PZT (61:39), PZT (52:48), and PZT (43:57). Lead acetate trihydrate [$\text{Pb}(\text{CH}_3\text{COO})_2 \cdot 3\text{H}_2\text{O}$], titanium isopropoxide [$\text{Ti}(\text{O}(\text{CH}_2\text{CH}_2\text{CH}_3)_2)_4$], and/or zirconium propoxide [$\text{Zr}(\text{O}(\text{CH}_2\text{CH}_2\text{CH}_3)_2)_4$] were dissolved into acetic acid (CH_3COOH) and 2-methoxyethanol ($\text{C}_3\text{H}_8\text{O}_2$) to form these solutions. A 1% volume proportion of methanamide is added to the solution as an adhesive to prevent micro-cracks in the film. Subsequently, the solutions were stirred for 4 h and aged for 72 h before spin-coating.

PbO , TiO_2 , and their mixture in an arbitrary ratio were spin-coated onto the substrates at 4000 rpm for 30 s, dried at 200 °C for 2 min, pyrolyzed at 380 °C for 5 min, and then annealed for crystallization at 700 °C for 10 min. This buffer layer is intended to construct textures, varying from [001], [011], to [111]. It is applied every ten PZT layers, ensuring effective structure constraints.

Subsequently, PbZrO_3 and PZT solutions can be spin-coated on the buffer layer at 4000 rpm for 30 s, dried at 200 °C for 2 min, pyrolyzed at 380 °C for 5 min, and then annealed for crystallization at 700 °C for 10 min. Single-composition $\text{Pb}(\text{Zr}_{0.52}\text{Ti}_{0.48})\text{O}_3$, with naturally occurring elemental segregation, was deposited to demonstrate the two-step strategy for attaining macroscopic piezoelectric response. Each layer is annealed separately with multiple repetitions to achieve the desired film thickness. To suppress elemental segregation, $\text{Pb}(\text{Zr}_{0.61}\text{Ti}_{0.39})\text{O}_3$ / $\text{Pb}(\text{Zr}_{0.52}\text{Ti}_{0.48})\text{O}_3$ / $\text{Pb}(\text{Zr}_{0.43}\text{Ti}_{0.57})\text{O}_3$ layers are periodically spin-coated. Each $\text{Pb}(\text{Zr}_{0.61}\text{Ti}_{0.39})\text{O}_3$ / $\text{Pb}(\text{Zr}_{0.52}\text{Ti}_{0.48})\text{O}_3$ /

$\text{Pb}(\text{Zr}_{0.43}\text{Ti}_{0.57})\text{O}_3$ period is annealed together as a unit. This determination considers the different nucleation and growth rates of Ti- and Zr-dominated regions. The relative rate for Zr crystallization is described by $r = \kappa_{\text{Zr}}/\kappa_{\text{Ti}}$, where κ_{Zr} and κ_{Ti} describe the specific growth speeds of Zr and Ti being integrated into the perovskite lattice from the amorphous phase²⁶. Previously, the relative rate coefficient r was estimated to be 0.70, where the Zr content at the beginning of growth passed from 52% Zr in the amorphous phase to 43% at the bottom of the crystallized layer. Therefore, a 61% Zr solution is required to obtain 52% Zr in the crystalline phase. To balance the final composition to 52:48, another 43% Zr composition should be incorporated. Therefore, a periodic Zr/Ti ratio from 61:39 to 52:48 to 43:57, considered as a unit, compensates for different growth rates and suppresses Zr/Ti segregation during crystallization. Hence, each of these three-layer periodic units is annealed together in the aforementioned high-temperature processing.

Room-temperature and high-temperature piezoelectricity measurements

The Pt electrode with a diameter of 2.5 mm was deposited on the PZT films by rf magnetron sputtering (VTC-2RF, MTI Corporation, China). For room-temperature piezoelectricity measurement, the sample is placed on a $5 \times 5 \text{ cm}^2$ silver platform (Supplementary Fig. 1a), which possesses a flatness of 0.1 mm. Pt in the Si/Pt/PZT wafer is wired to the silver platform as the bottom electrode. On top of the surface electrode, a metallic probe coated with Pt in a diameter of 2 mm applies small forces incrementally (such as 20, 40, 60, and 80 g) and measures the output voltage through the circuit, from which the piezoelectric coefficient can be fitted (Supplementary Fig. 1b). It should be noted that $d_{33,d}$ values measured on PZT ceramic with our instrument closely align with the values obtained using commercial d_{33} -meter, as shown in Supplementary Movie. 1, proving the validity of the measuring instrument. Therefore, this method has recently been proven effective for quantifying piezoelectricity with fine accuracy⁴⁶.

For in situ high-temperature measurements, the silver platform was used to heat the samples (Supplementary Fig. 1c), adopting a quarto temperature controller of LRT 001 (Gogo Instruments Technology, Shanghai, China). The heating rate can reach up to 100 °C/min, with a maximum temperature of 600 °C. Measurements are taken every 25 °C, allowing 10 min for stabilization at each temperature. A fixed K-type thermocouple is attached to the surface of the silver platform to record the operando temperature of the platform, whereas a mobile thermal meter (AS877, K-type, Smart Sensor) is contacted to the sample edge to ensure the alignment of the sample surface temperature with the silver platform. The electrical resistance of the silver platform changes from 0.5 to below 0.1 Ω as temperature increases from 25 to 500 °C, measured with a multimeter, ensuring superb contact of the sample bottom electrode. The temperature, force, and signal control are achieved by the software, as shown in Supplementary Fig. 1d. For the thermal fatigue measurements, a tube furnace is used to heat the Si/Pt/PZT sample to 400 °C, preserving 5 min for each cycle.

The dielectric constant, DC conductivity, depolarization behavior measured with 2.5 mm electrode pads

Adopting Pt electrode with a diameter of 2.5 mm, temperature-dependent dielectric constant at varied frequencies, for determining the phase-transition temperature, is measured using a dielectric spectroscopy test system (TZDM-RT-1000, Harbin Julang Technology Co., Ltd., China) and an LCR meter (E4980A, Agilent Corp., USA). It is also adopted for DC conductivity measurements. For the TSDC spectra, the sample is heated from 25 to 450 °C at a rate of 5 °C/min, and the depolarization current is recorded by a pA meter (6517B, Keithley, USA).

Ferroelectricity and dielectric constant measured with 200 μm electrode pad

The Au electrodes with a diameter of 200 μm were sputtered on the films, followed by baking at 200 $^{\circ}\text{C}$ for 15 min. The ferroelectric property as a function of field and temperature is measured by Multiferroic II (Radiant, USA) at a frequency of 5 kHz. The dielectric constant with continuous frequency change is measured by 4990 (Keysight, USA).

Converse piezoelectricity

The voltage-dependent displacement of the studied films under an electric bias was measured using a laser scanning vibrometer (LSV, PSV-400, OFV-3001-SF6, PolyTech GmbH, USA). A tungsten probe pin was used to apply the bias at the edge of the electrode, which has a diameter of 2.5 mm, consistent with that used for direct piezoelectricity measurements. The bottom electrode was grounded. Notably, only AC bias at amplitudes of 1–4 V with a frequency of 1 kHz was applied since the self-poled film does not require DC poling. During the measurement, a focused laser beam was directed at two regions on the thin film, covered and uncovered by the electrode, to measure the magnitude of the vibration. The displacement from the non-electrode area (i.e., the substrate displacement, δ_{sub}) was subtracted from the displacement of the film under the electrode (δ_{film}) to obtain the effective displacement, eliminating the substrate bending effect. To further minimize the substrate bending effect and mechanical resonance, the sample was affixed to the platform with silver paste.

Average structure and local domain structure

Theta-2theta X-ray diffraction (XRD) and ω -scan were carried out using a lab source with Cu-K α ($\lambda = 1.5406 \text{ \AA}$) radiation (D/max-2500, Rigaku, Tokyo, Japan). Electron backscattering diffraction (EBSD) is collected in Zeiss Auriga scanning electron microscopy. Raman spectra are excited by a 514.5 nm Ar⁺ laser (Raman spectrum, HORIBA, France). Atomic and piezoresponse force microscope (AFM and PFM) were performed in ambient conditions with an Infinity Asylum Research AFM. A Pt/Ir-coated tip on a Si cantilever (tip radius of 20 nm, force constant of 2.8 N/m, and a resonant frequency of 75 kHz) was used as movable top electrodes to conduct the bias. For the PFM mode, the PFM signal was collected at the contact resonance frequency with an AC tip bias of 1 V.

Atomic-scale image and elements characterization by using scanning transmission electron microscopy (STEM)

The TEM specimen consisted of a lamella extracted from the sample using focused-ion beam (FIB) milling carried out with a Zeiss Auriga FIB instrument. This lamella was then subjected to thinning to reduce the thickness of the surface amorphization layer, accomplished through ion beam milling using a 5 kV, 20 mA setting. Subsequently, meticulous thinning and polishing of the TEM sample were performed using a Nanomill instrument. For investigations into the atomic structure and element mapping characterization, scanning transmission electron microscopy (STEM) was employed. This was conducted on an FEI Titan Cubed Themis G2 300 operating at 300 kV. The microscope was equipped with a high-brightness Schottky field emission gun and monochromator, as well as a probe aberration corrector that provided exceptional spatial resolution, surpassing 0.6 \AA in STEM mode. An energy-dispersive EDS detector was also part of the setup. To achieve atomic number (Z) contrast imaging, the high-angle annular dark-field (HAADF) mode was utilized, featuring a probe convergence angle of 25 mrad, and inner collection and outer collection angles of approximately 80 mrad and 240 mrad, respectively. EDS was combined with HAADF imaging to facilitate element mapping. In the case of nanobeam diffraction, 4D datasets were acquired. These datasets were captured

using an electron microscope pixel array detector (EMPAD) attached to a probe aberration-corrected FEI Titan Cubed Themis G2. The convergence semi-angle for this setup was approximately 0.5 mrad, and each diffraction pattern obtained had dimensions of 128 \times 128. To determine atomic column positions within the HAADF images and extract the local lattice parameters and relative atomic displacement, a 2D Gaussian fitting method was employed within Matlab software.

Phase field simulation of composition gradient ferroelectric films

In the phase field simulation of the composition gradient PZT film, the evolution of the polarization was achieved by solving the time-dependent Ginzburg-Landau (TDGL) equation:

$$\frac{\partial P_i(\mathbf{r}, t)}{\partial t} = -L \frac{\delta F}{P_i(\mathbf{r}, t)} \quad (i=1, 2, 3) \quad (1)$$

where L denotes the kinetic coefficient, \mathbf{r} is the spatial position vector, and t represents the evolution time. The total free energy F is a sum of the Landau free energy, elastic energy, electrostatic energy, gradient energy, and flexoelectric energy, that is:

$$F = \int (f_{\text{Landau}} + f_{\text{elastic}} + f_{\text{electric}} + f_{\text{gradient}} + f_{\text{flexoelectric}}) dV \quad (2)$$

The formula of each free energy density can be found in literature^{47–50}. The Landau free energy parameters in terms of the Pb(Zr_{1-x}Ti_x)O₃ composition x are obtained from Ref. 51

$$\begin{aligned} \alpha_1 &= (T - T_0)/2\epsilon_0 C_0, \quad \epsilon = 8.85 \times 10^{-12} \\ \alpha_{11} &= (10.612 - 22.655x + 10.955x^2) \times 10^{13}/C_0 \\ \alpha_{111} &= (12.026 - 17.296x + 9.179x^2) \times 10^{13}/C_0 \\ \alpha_{112} &= (4.2904 - 3.3754x + 58.804e^{-29.397x}) \times 10^{14}/C_0 \\ \alpha_{12} &= \eta_1/3 - \alpha_{11}, \quad \alpha_{123} = \eta_2 - 3\alpha_{111} - 6\alpha_{112} \\ \eta_1 &= [2.6213 + 0.42743x - (9.6 + 0.012501x)e^{-12.6x}] \times 10^{14}/C_0 \\ \eta_2 &= [0.887 + 0.76973x + (16.225 - 0.088651x)e^{-21.255x}] \times 10^{15}/C_0 \\ T_0 &= 462.63 + 843.4x - 2105.5x^2 + 4041.8x^3 - 3828.3x^4 + 1337.8x^5 \\ C_0 &= \left(\frac{2.1716}{1 + 500.05(x - 0.5)^2} + 0.131x + 2.01 \right) \times 10^5, \text{ when } 0.0 \leq x \leq 0.5 \\ C_0 &= \left(\frac{2.8339}{1 + 126.56(x - 0.5)^2} + 1.4132 \right) \times 10^5, \text{ when } 0.5 \leq x \leq 1.0 \\ Q_{11} &= \frac{0.029578}{1 + 200(x - 0.5)^2} + 0.042796x + 0.045624 \\ Q_{12} &= \frac{0.026568}{1 + 200(x - 0.5)^2} + 0.012093x - 0.013386 \\ Q_{44} &= \frac{1}{2} \left(\frac{0.025325}{1 + 200(x - 0.5)^2} + 0.020857x + 0.046147 \right) \end{aligned} \quad (3)$$

where α_s are the Landau coefficients, T_0 is the Curie temperature, and Q_s represent the electrostrictive coefficients. The numerical solution of the phase field model was performed utilizing the finite element method. As estimated from the experimental data, the composition x of each 100 nm PZT layer of the film linearly changes from 0.5 at the bottom to 0.35 at the top surface. As the lattice constant of PZT increases with the decrease of Ti content, an in-plane strain gradient of ~3% can be induced due to the composition of graded heterostructures. Such a strain gradient induces a built-in electric field which could lead to the spontaneous orientation of the polarization.

Reporting summary

Further information on research design is available in the Nature Portfolio Reporting Summary linked to this article.

Data availability

All data supporting the results of this study are available in the manuscript or the supplementary information. All related data are accessible in figshare⁵².

References

1. Kanno, I. Piezoelectric MEMS: Ferroelectric thin films for MEMS applications. *Jpn. J. Appl. Phys.* **57**, 040101 (2018).
2. Baek, S. H. et al. Giant piezoelectricity on Si for hyperactive MEMS. *Science* **334**, 958 (2011).
3. Eom, C.-B. & Trolrier-McKinstry, S. Thin-film piezoelectric MEMS. *MRS Bull.* **37**, 1007 (2012).
4. Paull, O. et al. Anisotropic epitaxial stabilization of a low-symmetry ferroelectric with enhanced electromechanical response. *Nat. Mater.* **21**, 74–80 (2022).
5. Hu, H. et al. A wearable cardiac ultrasound imager. *Nature* **613**, s41586 (2023).
6. Wang, H. S. et al. Biomimetic and flexible piezoelectric mobile acoustic sensors with multiresonant ultrathin structures for machine learning biometrics. *Sci. Adv.* **7**, <https://doi.org/10.1126/sciadv.abe5683> (2021).
7. Wang, C. et al. Bioadhesive ultrasound for long-term continuous imaging of diverse organs. *Science* **377**, 517–523 (2022).
8. Yi, Z. et al. Piezoelectric dynamics of arterial pulse for wearable continuous blood pressure monitoring. *Adv. Mater.* **34**, 2110291 (2022).
9. Zhang, T. et al. Piezoelectric ultrasound energy-harvesting device for deep brain stimulation and analgesia applications. *Sci. Adv.* **8**, eabk0159 (2022).
10. Park, G.-T., Park, C.-S., Choi, J.-J., Lee, J.-W. & Kim, H.-E. Effects of thickness on piezoelectric properties of highly oriented lead zirconate titanate films. *J. Am. Ceram. Soc.* **89**, 2314–2316 (2006).
11. Park, G.-T., Park, C.-S., Choi, J.-J. & Kim, H.-E. Orientation control of sol-gel-derived lead zirconate titanate film by addition of polyvinylpyrrolidone. *J. Mater. Res.* **20**, 882–888 (2005).
12. Xu, F., Chu, F. & Trolrier-McKinstry, S. Longitudinal piezoelectric coefficient measurement for bulk ceramics and thin films using pneumatic pressure rig. *J. Appl. Phys.* **86**, 588–594 (1999).
13. Li, J. et al. Lead zirconate titanate ceramics with aligned crystallite grains. *Science* **380**, 87–93 (2023).
14. Zhao, D. et al. Depolarization of multidomain ferroelectric materials. *Nat. Commun.* **10**, 2547 (2019).
15. Kholkin, A. L., Brooks, K. G., Taylor, D. V., Hiboux, S. & Setter, N. Self-polarization effect in Pb(Zr, Ti)O₃ thin films. *Integr. Ferroelectr.* **22**, 525–533 (1998).
16. Osipov, V. V., Kaptelov, E. Y., Senkevich, S. V., Kiselev, D. A. & Pronin, I. P. The study of self-poled PZT thin films under variation of lead excess. *Ferroelectrics* **525**, 76–82 (2018).
17. Liu, Y. et al. All-ceramic flexible piezoelectric energy harvester. *Adv. Funct. Mater.* **32**, 2209297 (2022).
18. Mangalam, R. V. K., Karthik, J., Damodaran, A. R., Agar, J. C. & Martin, L. W. Unexpected crystal and domain structures and properties in compositionally graded PbZr_{1-x}Ti_xO₃ thin films. *Adv. Mater.* **25**, 1761–1767 (2013).
19. Zou, D. et al. Flexible and translucent PZT films enhanced by the compositionally graded heterostructure for human body monitoring. *Nano Energy* **85**, 105984 (2021).
20. Zhao, J. et al. Recoverable self-polarization in lead-free bismuth sodium titanate piezoelectric thin films. *ACS Appl. Mater. Interfaces* **9**, 28716–28725 (2017).
21. Zhao, J. et al. Self-polarization in epitaxial fully matched lead-free bismuth sodium titanate based ferroelectric thin films. *ACS Appl. Mater. Interfaces* **10**, 23945–23951 (2018).
22. Hiboux, S. & Mural, P. Mixed titania-lead oxide seed layers for PZT growth on Pt(111): a study on nucleation, texture and properties. *J. Eur. Ceram. Soc.* **24**, 1593–1596 (2004).
23. Gong, W., Li, J.-F., Chu, X., Gui, Z. & Li, L. Combined effect of preferential orientation and Zr/Ti atomic ratio on electrical properties of Pb(Zr_xTi_{1-x})O₃ thin films. *J. Appl. Phys.* **96**, 590 (2004).
24. Mhin, S. et al. Role of the PbTiO₃ seed layer on the crystallization behavior of PZT thin films. *J. Am. Ceram. Soc.* **98**, 1407–1412 (2015).
25. Li, F., Zhang, S., Damjanovic, D., Chen, L.-Q. & Shrout, T. R. Local structural heterogeneity and electromechanical responses of ferroelectrics: Learning from relaxor ferroelectrics. *Adv. Funct. Mater.* **28**, 1801504 (2018).
26. Calame, F. & Mural, P. Growth and properties of gradient free sol-gel lead zirconate titanate thin films. *Appl. Phys. Lett.* **90**, 062907 (2007).
27. You, L. et al. Origin of giant negative piezoelectricity in a layered van der Waals ferroelectric. *Sci. Adv.* **5**, eaav3780 (2019).
28. Kanno, I., Kotera, H. & Wasa, K. Measurement of transverse piezoelectric properties of PZT thin films. *Sens. Actuators A* **107**, 68–74 (2003).
29. Watanabe, H., Yamada, N. & Okaji, M. Linear thermal expansion coefficient of silicon from 293 to 1000 K. *Int. J. Thermophys.* **25**, 221–236 (2004).
30. Sato, Y., Kimura, G., Kweon, S. H., Tan, G. & Kanno, I. Disruption of polar order in lead zirconate titanate by composition-modulated artificial superlattice. *J. Mater. Sci.* **59**, 8134–8146 (2024).
31. Zhao, J. et al. Recoverable self-polarization in lead-free bismuth sodium titanate piezoelectric thin films. *ACS Appl. Mater. Interfaces* **10**, 23945–23951 (2018).
32. Shepard, J. F. Jr., Chu, F., Moses, P. J. & Trolrier-McKinstry, S. The influence of film thickness on the magnitude and aging behavior of the transverse piezoelectric coefficient (D31) of Pzt thin films. *Mat. Res. Soc. Symp. Proc.* **493**, 415 (1998).
33. Wolf, R. A. & Trolrier-McKinstry, S. Temperature dependence of the piezoelectric response in lead zirconate titanate films. *J. Appl. Phys.* **95**, 1397–1406 (2004).
34. Rossel, C. et al. Temperature dependence of the transverse piezoelectric coefficient of thin films and aging effects. *J. Appl. Phys.* **115**, 034105 (2014).
35. Kim, D.-S. et al. Remarkable piezoelectric performance and good thermal stability of <001>-textured 0.96(K_{0.5}Na_{0.5})(Nb_{1-y}Sb_y)O₃-0.04SrZrO₃ lead-free piezoelectric ceramics. *J. Alloy. Compd.* **882**, 160662 (2021).
36. Park, J. H., Xu, F. & Trolrier-McKinstry, S. Dielectric and piezoelectric properties of sol-gel derived lead magnesium niobium titanate films with different textures. *J. Appl. Phys.* **89**, 568–574 (2001).
37. Liu, Y. et al. Ferroelectric polymers exhibiting behaviour reminiscent of a morphotropic phase boundary. *Nature* **562**, 96 (2018).
38. Hu, X., You, M., Yi, N., Zhang, X. & Xiang, Y. Enhanced piezoelectric coefficient of PVDF-TrFE films via in situ polarization. *Front. Energy Res.* **9**, 621540 (2021).
39. Huang, Z.-X. et al. Self-poled piezoelectric polymer composites via melt-state energy implantation. *Nat. Commun.* **15**, 819 (2024).
40. Khomyakova, E. et al. Self-poling of BiFeO₃ thick films. *ACS Appl. Mater. Interfaces* **8**, 19626–19634 (2016).
41. Zhang, T., Wasa, K., Kanno, I. & Zhang, S.-Y. Ferroelectric properties of Pb(Mn_{1/3}Nb_{2/3})O₃-Pb(Zr, Ti)O₃ thin films epitaxially grown on (001) MgO substrates. *J. Vac. Sci. Technol. A* **26**, 985 (2008).
42. Han, G. et al. Stress-controlled Pb(Zr_{0.52}Ti_{0.48})O₃ thick films by thermal expansion mismatch between substrate and Pb(Zr_{0.52}Ti_{0.48})O₃ film. *J. Appl. Phys.* **110**, 124101 (2011).

43. Murlalt, P. PZT Thin films for microsensors and actuators: Where do we stand? *IEEE T Ultrason. Ferr.* **47**, 903–915 (2000).
 44. Nguyen, M. D., Houwman, E. P. & Rijnders, G. Large piezoelectric strain with ultra-low strain hysteresis in highly c-axis oriented $\text{Pb}(\text{Zr}_{0.52}\text{Ti}_{0.48})\text{O}_3$ films with columnar growth on amorphous glass substrates. *Sci. Rep.* **7**, 12915 (2017).
 45. Wang, S. et al. Element segregation and electrical properties of PMN-32PT grown using the bridgman method. *Crystals* **9**, 98 (2019).
 46. Chen, C. et al. A method for quantitatively separating the piezoelectric component from the as-received “Piezoelectric” signal. *Nat. Commun.* **13**, 1391 (2022).
 47. Chen, H. T., Soh, A. K. & Ni, Y. Phase field modeling of flexoelectric effects in ferroelectric epitaxial thin films. *Acta Mech.* **225**, 1323–1333 (2014).
 48. Liu, Z., Yang, B., Cao, W. & Lookman, T. Effect of misfit strain on ferroelectric domain formation at the morphotropic phase boundary. *Phys. Rev. B* **94**, 214117 (2016).
 49. Liu, Z., Zhou, X., Feng, B. & Xu, B.-X. Engineered periodic quadrupole superstructure in ferroelectric thin films via flexoelectricity. *Acta Mater.* **216**, 117126 (2021).
 50. Chen, L.-Q. Phase-field method of phase transitions/domain structures in ferroelectric thin films: A review. *J. Am. Ceram. Soc.* **91**, 1835–1844 (2008).
 51. Rabe, K. M. *Physics of Ferroelectrics: A Modern Perspective*. (Springer Science & Business Media, 2007).
 52. Liu, L. et al. High piezoelectric property with exceptional stability in self-poled ferroelectric films. *Figshare, Dataset* (2024).
- the electrodes and carried out piezoelectricity measurements. J.F.L. and S.Z. guided the work and analyzed the piezoelectric results. L.L., J.Y., K.X., S.Z., and Y.W. wrote and revised the manuscript with input from others. All authors discussed the results, commented on the manuscript, and acknowledged their inclusion and contribution to the current manuscript.

Competing interests

The authors declare no competing interests.

Additional information

Supplementary information The online version contains supplementary material available at <https://doi.org/10.1038/s41467-024-54707-y>.

Correspondence and requests for materials should be addressed to Lisha Liu, Jiaojiao Yi, Shujun Zhang or Yaojin Wang.

Peer review information *Nature Communications* thanks the anonymous reviewer(s) for their contribution to the peer review of this work. A peer review file is available.

Reprints and permissions information is available at <http://www.nature.com/reprints>

Publisher’s note Springer Nature remains neutral with regard to jurisdictional claims in published maps and institutional affiliations.

Open Access This article is licensed under a Creative Commons Attribution-NonCommercial-NoDerivatives 4.0 International License, which permits any non-commercial use, sharing, distribution and reproduction in any medium or format, as long as you give appropriate credit to the original author(s) and the source, provide a link to the Creative Commons licence, and indicate if you modified the licensed material. You do not have permission under this licence to share adapted material derived from this article or parts of it. The images or other third party material in this article are included in the article’s Creative Commons licence, unless indicated otherwise in a credit line to the material. If material is not included in the article’s Creative Commons licence and your intended use is not permitted by statutory regulation or exceeds the permitted use, you will need to obtain permission directly from the copyright holder. To view a copy of this licence, visit <http://creativecommons.org/licenses/by-nc-nd/4.0/>.

© The Author(s) 2024

Acknowledgements

L.L. acknowledges discussions on film fabrications with Xianfeng Chen, affiliated with Zilm Co. Ltd., and the National Center for Electron Microscopy in Beijing. This work was supported by The National Natural Science Foundation of China (52072178, 52102133) (Y.W. and L.L.), The Natural Science Foundation of Jiangsu Province, China (BK20210354) (L.L.), The Fundamental Research Funds for the Central Universities (30921011217, 30920041119) (L.L. and Y.W.), The Basic Science Center Project of National Natural Science Foundation of China (52388201) (J.F.L.), The Basic and Applied Basic Research Major Program of Guangdong Province, China (2021B0301030003) and Jihua Laboratory (X210141TL210) (K.X.)

Author contributions

L.L. and Y.W. conceived the main idea, grew the films, performed X-ray diffraction, and regulated the film texture. J.Y. carried out the electric and ferroelectric testing and the analysis. K.X. performed aberration-corrected STEM and analyzed the data. Z.L. performed and analyzed the COMSOL simulations. M.T., L.D., X.G., Y. L., S.W., Z.Z. and L.S. deposited